

principal component decomposition to high resolution time series from the region produced by the advanced Multidimensional SBAS DInSAR technique in order to better delineate both the deeper source and the recent shallow activity. We analyzed both a period of substantial subsidence (1993-1999) and a second of significant uplift (2007-2013) and inverted the associated vertical surface displacement for the most likely source models. Results suggest that the underlying dynamics of the caldera changed in the late 1990s, from one in which the primary signal arises from a shallow deflating source above a deeper, expanding source to one dominated by a shallow inflating source. In general, the shallow source lies between 2700 and 3400 m below the caldera while the deeper source lies at 7600 m or more in depth. The combination of principal component analysis with high resolution MSBAS time series data allows for these new insights and confirms the applicability of both to areas at risk from dynamic natural hazards.

1. Introduction

A significant portion of the city of Naples lies within the Campi Flegrei caldera, along with the town of Pozzuoli and a number of densely inhabited villages, making it one of the most dangerous volcanic areas on Earth (Orsi et al., 2004; De Natale et al., 2006; Isaia et al., 2009). The last major eruption occurred at Monte Nuovo in 1538, following a period of ground uplift which interrupted a period of secular subsidence that has persisted for centuries. During that time, Campi Flegrei has undergone frequent episodes of ground subsidence and uplift accompanied by seismic activity (Troise et al., 2007). Most recently, in June of 2010 moderate uplift rates were observed that substantially increased in 2011 and further accelerated in 2012. Between 2010 and 2013, maximum uplift reached approximately 13 cm, as identified by differential Interferometric Synthetic Aperture Radar (DInSAR) (Samsonov et al., 2014b).

DInSAR is used extensively today for mapping ground deformation with high spatial resolution and sub-centimeter precision over large areas, and is a suitable tool for deformation monitoring of active volcanic areas (Massonnet and Feigl, 1998; Rosen et al., 2000; Wadge, 2003; Fernández et al., 2009). A radar interferogram is calculated from two SAR images with identical characteristics acquired by space- and/or air-borne sensors at two different times and captures the intervening deformation. Spatial resolution of modern SAR sensors ranges from 1 to 20 m over areas from 10 x 10 km to approximately 200 x 200 km. For modern satellite constellations the repeat cycle ranges from a few days to a few weeks, with the typical repeat cycle for a single satellite mission at 24 to 41 days. Repeatedly acquired SAR data from a single sensor can be used to obtain line-of-sight (LOS) time series analysis of surface displacement through the application of either Small Baseline Subset (SBAS) (Berardino et al., 2002; Usai, 2003; Samsonov et al., 2011), Persistent Scatterers (PS) (Ferretti et al., 2001) methods or their combination (Hooper, 2008). The results are limited to the time period of the individual data set and do not automatically distinguish between horizontal and vertical motion.

The Multidimensional SBAS (MSBAS) technique (Samsonov and d'Oreye, 2012) combines multiple DInSAR data sets into a single solution. Improved characteristics include lower noise and improved temporal resolution with almost uninterrupted temporal coverage. The MSBAS methodology is an extension of the original SBAS method. MSBAS addresses the data redundancy and multidimensionality of the problem by decomposing LOS DInSAR measurements into the vertical and horizontal (east-west) time series of surface deformation using ascending and descending DInSAR data. MSBAS recently has been applied to the mapping of anthropogenic (Samsonov et al., 2013, 2014a) and natural (Samsonov and d'Oreye,

2012; Samsonov et al., 2014b) ground deformation, successfully producing two-dimensional time series with dense temporal resolution and high precision.

In this study we apply a principal component decomposition technique to an MSBAS DInSAR time series of more than twenty years, produced from ERS-1/2, ENVISAT and RADARSAT-2 data at Campi Flegrei, Italy (Figure 1) (Samsonov et al., 2014b). Various versions of principal component analysis (PCA) filtering techniques have been developed and applied over the past 28 years with the goal of reducing or removing the various noise sources in the position time series.

For example, in the first successful geodetic application, Savage (1988) decomposed displacements at Long Valley caldera into the predominant modes in order to study only the signal that accounted for the greatest percentage of the variance, the volcanic source below the dome. In addition, he identified the primary error sources in the data using the remaining eigenmodes. Tiampo et al. (2004) employed a Karhunen-Loeve expansion (KLE) analysis to study spatiotemporally correlated mass loading caused by seasonal deformation in Southern California Integrated GPS Network (SCIGN) position series data. Dong et al. (2006) later employed common mode error (CME) filtering using both PCA and KLE techniques in order to identify signal and systematic error in regional GPS position time series. Zerbini et al. (2010) applied a similar technique to GPS and gravity data in northeastern Italy and succeeded in identifying hydrology-related correlated variations, while Chaussard et al. (2014) used a PCA decomposition of DInSAR data to study aquifer changes in northern California. Here, because the MSBAS data produces a time series with unprecedented duration and resolution for this region, the PCA produces individual spatial and temporal modes at high resolution in both space and time. Various combinations of the resulting eigenmodes are inverted using a genetic algorithm (GA) inversion technique and a combination of simple spherical pressure models

(Mogi, 1958). The combination of these three techniques – MSBAS DInSAR, PCA decomposition and GA inversion - results in the improved characterization of the two separate sources below Campi Flegrei and new insights into the interactions between the deeper source and the recent shallow activity. Results suggest that the underlying dynamics of the caldera changed in the late 1990s, from one in which the primary signal arises from a shallow deflating source above a deeper, expanding source to one dominated by a shallow inflating source.

In Section 2 we provide an overview of historic activity at Campi Flegrei. Section 3 provides details on the MSBAS technique and the SAR data used in this study. Section 4 describes the PCA technique and the resulting decomposition of the MSBAS time series into their eigenmodes and principal components. The GA inversion technique and its application to the significant eigenmodes are detailed in Section 5. The last section discusses the results and implications of this analysis for constraining different geophysical sources at Campi Flegrei.

2. Campi Flegrei

The Campi Flegrei caldera (Figure 1), located east of the city of Naples in southern Italy, was formed by two major eruptions at 35 and 15 ka (Rosi et al., 1983). In modern times, a significant eruption occurred in 1538 and, since then, Campi Flegrei caldera has undergone frequent episodes of ground subsidence and uplift accompanied by seismic activity (Troise et al., 2007). Di Vito et al. (2016) has interpreted pre-eruptive magma transfer since 1538 as the result of a stationary oblate source deeper below the caldera that has been feeding shallower sources and eruptions for the last 5 ka.

The most recent uplift probably began in 1950 and included two major periods of seismic unrest in 1969–1972 and 1982–1984, before reaching a maximum value of about 3.5 m in 1985 (Gottsmann et al., 2006; Del Gaudio et al., 2010; D’Auria et al., 2011). Since 1988, slow

deflation intermittently has been interrupted by periods of seismic swarms and minor uplift, until the mid-2000s (Trasatti et al., 2015). At that time, a significant increase in the uplift rate took place, resulting in almost 13 cm of uplift by 2013 (De Martino et al., 2014; Samsonov et al., 2014b).

FIGURE1

Between 1981 and 2001, surveys at Campi Flegrei revealed significant gravity changes. Interpretation, in conjunction with deformation data, suggested that the phenomena are the result of changes in the caldera hydrothermal systems (Bonafede & Mazzanti, 1998; Camacho et al., 2011), activity within the subsurface magmatic reservoir (Dvorak & Berrino, 1991; Fernández et al., 2001), or some combination of the two (Gottsmann et al., 2005, 2006). Recent petrological and geochemical studies suggest that there are two magmatic sources that differ in composition, depth and size, and that the periodic episodes of uplift and unrest are the result of reinjection of CO₂-rich fluids and magma (Caliro et al., 2007; Arienzo et al., 2010; Mormone et al., 2011; D'Auria et al., 2011, 2012; Moretti et al., 2013; Amoruso et al., 2014a; Trasatti et al., 2015). Over the years, a number of different models have been ascribed to the shallow source, or sources, at Campi Flegrei. These generally include a primary inflation source between 2-4 km in depth below the caldera and some combination of shallower hydrothermal sources near the Solfatara crater (De Natale et al. 1991, De Natale et al., 2006; Gottsmann et al., 2005, 2006; Amoruso et al., 2008; Camacho et al., 2011; Trasatti et al., 2011; Amoruso et al., 2014a; Samsonov et al., 2014b; Trasatti et al., 2015, among others), although some studies have attributed CF activity primarily to fluid injection in the hydrothermal system (Battaglia et al.,

2006; Troiano et al., 2011). Battaglia et al. (2006) inverted levelling, trilateration and gravity from the period between 1980 and 1995 and found that the inflation period during the 1980s was the result of a penny-shaped crack at a depth of approximately 3 km and the subsequent deflation was generated by a source shaped like a prolate spheroid at a depth between 1.9 and 2.2 km deep. More recently, Amoroso et al. (2015) modeled observed strain changes from March of 2010 as the result of volume changes in an offshore, slightly deeper ellipsoidal magma source at approximately 3200 m depth.

Tomographic studies suggest that there is a high V_p/V_s ratio at shallow depths, indicating infiltration by hydrothermal fluids (Chiarabba and Moretti, 2006; Zollo et al., 2008). Seismic attenuation results also identify potential melt volumes at a depth of approximately 3500 and 7500 m below the caldera (De Siena et al., 2010). The models of Trasatti et al. (2011) suggest that this shallower source is fed by a deep sill, again at approximately 7500 m in depth. The recent ground deformation, 2012-2013, was modeled using DInSAR and GPS measurements as the result of a sill-like magma intrusion at approximately 3090 meters in depth (D'Auria et al., 2015), while Amoroso et al. (2014b) demonstrated that a deeper source (~3600 m), combined with the shallower Solfatara hydrothermal source, can explain the continuous GPS (cGPS) displacements since 2011. Both the subsidence period of 1993-1999 and the more recent uplift, 2007–2013, were modeled, again using DInSAR data, as the result of activity in an extended source at depths of approximately 1400 to 2000 m depth (Samsonov et al. 2014b).

Here we apply a PCA decomposition technique (Tiampo et al., 2012) and a GA inversion method to the DInSAR MSBAS data of Samsonov et al. (2014) in order to better discriminate between the potential sources at Campi Flegrei.

3. MSBAS Analysis

The theoretical derivation of the MSBAS technique is described in detail in Samsonov and d'Oreye (2012) and Samsonov et al. (2013). The technique is derived from the original SBAS method proposed in Berardino et al. (2002) and Usai (2003) but incorporates images from different satellites, coverage and look angles in order to produce two-dimensional time series of ground deformation. At least two sets of DInSAR data are needed, one from ascending and the other from descending orbits. The technique, however, efficiently handles a large number of DInSAR data sets to produce results with improved temporal resolution and precision. Basic DInSAR processing is performed outside of the MSBAS software, using either freely available (e.g. ISCEE, GMT5SAR) or commercial (GAMMA, SARscape) packages. Differential interferograms are processed, filtered, unwrapped and geocoded with the processing software and then resampled to a common grid. The final interferograms are in either angular (e.g. radian) or metric (e.g. cm or m) units, preserved during the MSBAS processing. The topographic correction is accomplished by a joint inversion that solves for the two-dimensional displacements and the residual topographic signal (Samsonov et al., 2011). The resulting deformation maps presented in this work were calculated from two decades of SAR measurements from three different SAR sensors (ERS-1/2, ENVISAT and RADARSAT-2). Individual frames are shown in Figure 1.

We processed five independent SAR data sets, described in Table 1, with uninterrupted coverage from 1992 through 2013. We applied 2x10 multilooking to four standard beams and 4x5 multilooking to one fine beam and independently processed each data set using GAMMA software (Wegmuller and Werner, 1997). All possible interferometric pairs with perpendicular baselines less than 400 m were computed and the topographic signal was removed using a 90 m resolution SRTM DEM (Farr and Kobrick, 2000). Orbital refinement to remove residual orbital

ramps was performed and minor interpolation applied to fill gaps in moderately coherent regions.
The final interpolated interferograms were geocoded onto a 90x90 m grid.

TABLE 1

For the time series analysis we limited data to the Naples Bay area and resampled all interferograms to a common grid (Wessel and Smith, 1998). The final interferograms had a resolution of approximately 90x90 m. We selected only those with an average coherence above 0.5 for further processing. Over one thousand highly coherent interferograms then were used in the MSBAS processing, resulting in a time series with 385 time steps. Average error on the vertical and east-west displacement time series is approximately 0.1 cm (Samsonov et al., 2014b).

The results of the MSBAS processing are presented in Figure 2. Figure 2a shows the vertical change in surface height between the initial and final time steps while Figure 2b is the east-west net displacement. The associated displacement time series are shown in Figure 2c for the location designated with the pink star. They present a more complicated picture than the net displacement of Figures 2a and 2b. The time series show more than 3 cm/yr of maximum subsidence (green dot) between 1993 and 1999, centered on the caldera. Subsidence continued at a slower rate, interspersed with short periods of uplift, until 2005. Almost continuous uplift began in 2005 and accelerated to approximately 2.5 cm/yr between 2008 and 2011. Deformation is ongoing at a rate of 5 cm/yr (2011–2013). The large number of time steps and precise measurements are evident in both the vertical and east-west time series (Figure 2c). The pattern

of deformation in Figure 2 is consistent with one or more sources of contraction and expansion located at depth below the caldera.

FIGURE 2

Figure 3 shows the net surface displacement for two different time periods, 1993 through 1999 and 2007 through 2013. The subsidence that occurred between 1993 and 1999 can be seen in Figure 3a, while the corresponding east-west displacement is provided in Figure 3b. Figure 3c presents the uplift for the period of 2007-2013 and Figure 3d shows the associated east-west displacements.

FIGURE3

4. PCA Analysis

The Karhunen-Loeve expansion (KLE) method is a linear decomposition technique in which a dynamical system is decomposed into a complete set of orthonormal subspaces. Depending on the specific decomposition, and whether it is used to characterize the variance or correlation in the data, it also has been known as PCA or empirical orthogonal function (EOF) decomposition. The method, in one form or another, has been applied to a number of complex nonlinear systems over the last fifty years, including the ocean-atmosphere interface, turbulence, meteorology, biometrics, statistics, and geophysics (Hotelling, 1933; Fukunaga, 1970; Aubrey and Emery, 1983; Preisendorfer, 1988; Savage, 1988; Penland, 1989; Vautard and Ghil, 1989; Posadas et al., 1993; Penland and Sardeshmukh, 1995; Holmes et al., 1996; Moghaddam et al., 1998; Tiampo et al., 2002; Dong et al., 2006; Main et al., 2006; Small and Islam, 2007; Smith et al., 2007). Again, Savage (1988) decomposed the deformation at Long Valley caldera into its predominant modes in order to study only the signal that accounted for the greatest percentage of the variance,

237 the volcanic source below the dome. In addition, he identified the primary error sources in the
238 data using the remaining eigenmodes.

239 In an application of the KLE to historic seismicity data, Tiampo et al. (2002) constructed a
240 correlation operator, $C(x_i, x_j)$, for seismic events over time. Subsequently, $C(x_i, x_j)$ was
241 decomposed into its orthonormal spatial eigenmodes and associated time series, $a_j(t)$. These
242 spatial and temporal pattern states were used to reconstruct the primary modes of the system,
243 with or without noise, and to characterize the underlying dynamics and the physical parameters
244 that control the observable patterns of events. The decomposition implicitly assumes that one is
245 dealing with a process that is both Markov and stationary in time. Anghel et al. (2004) applied a
246 similar methodology to modeled deformation data with the goal of identifying coherent
247 structures and interactions. Tiampo et al. (2004) applied the KLE technique to SCIGN data in
248 order to determine the principal modes of deformation for the southern California fault system,
249 while Dong et al. (2006) applied a similar technique to SCIGN data in order to study the CME.
250 More recently, it has been applied to DInSAR time series studies, primarily for better
251 understanding of volcanic and groundwater changes (Lipovsky, 2011; Rudolph et al., 2013;
252 Chaussard et al., 2014; Remy et al., 2014).

253 As with the EOF technique developed by Preisendorfer (1988) for the atmospheric sciences, the
254 KLE for displacement applications uses those p time series that record the deformation history at
255 particular locations in space. The primary difference is that while an EOF decomposition is
256 based on the covariance matrix, a KLE decomposition is performed on a correlation operator
257 (Fukunaga, 1970). For the study at Campi Flegrei, we employ an EOF operator.

Each time series, $y(x_s, t_i) = y_i^s$, $s = 1, \dots, p$, consists of n time steps, $i = 1, \dots, n$. The goal is to construct a time series for each of a large number of locations for a given short period of time. If, for example, the time interval was decimated into units of days, the result could be a time series of 365 time steps for every year of data, with values of position for that location at each time step. These time series are incorporated into a matrix, \mathbf{T} , consisting of time series of the same measurement for p different locations, i.e.

$$\mathbf{T} = [\bar{y}_1, \bar{y}_2, \dots, \bar{y}_p] = \begin{bmatrix} y_1^1 & y_1^2 & \dots & y_1^p \\ y_2^1 & y_2^2 & \dots & y_2^p \\ \vdots & \vdots & \ddots & \vdots \\ y_n^1 & y_n^2 & \dots & y_n^p \end{bmatrix}. \quad (1)$$

For analysis of DInSAR data, the values in the matrix \mathbf{T} consist of horizontal or vertical position measurements. The covariance matrix, $S(x_i, x_j)$, for these events is formed by multiplying \mathbf{T} by \mathbf{T}^T , where S is a $p \times p$ real, symmetric matrix.

This equal-time covariance operator, $S(x_i, x_j)$, is decomposed into its eigenvalues and eigenvectors in two parts. The first employs the triredution technique to reduce the matrix S to a symmetric tridiagonal matrix, using a Householder reduction. The second part employs a QL algorithm to find the eigenvalues, λ_j , and eigenvectors, e_j , of the tridiagonal matrix (Press, et al., 1992). These eigenvectors, or eigenstates, are orthonormal basis vectors arranged in order of decreasing variance that reflect the spatial relationship of events in time. If one divides the corresponding eigenvalues, λ_j , by the sum of the eigenvalues, the result is that percent of the correlation accounted for by that particular mode. We then reconstruct the time series associated with each location for each eigenstate by projecting the initial data back onto these basis vectors in what is called a PC analysis (Preisendorfer, 1988). These time dependent expansion

coefficients, $a_j(t)$, which represent the temporal eigenvectors, are reconstructed by multiplying the original data matrix by the eigenvectors, i.e.

$$a_j(t_i) = \vec{e}^T \cdot \mathbf{T} = \sum_{s=1}^p e_j y_i^s, \quad (2)$$

where $j, s = 1, \dots, p$ and $i = 1, \dots, n$. This eigenstate decomposition technique produces the orthonormal spatial eigenmodes for this nonlinear threshold system, e_j , and the associated principal component time series, $a_j(t)$. These principal component time series represent the signal associated with each particular eigenmode over time. For purposes of clarity, the spatial eigenvectors are designated EOF modes and the associated time series are the principal component analysis (PCA) vectors.

PCA often is used to filter data through the identification of those modes associated with large percentages of unwanted covariance or those lower modes accounting for random noise (Preisendorfer, 1988; Penland, 1989; Dong et al., 2006). As discussed above, others have applied the technique to investigate spatiotemporally correlated geophysical signals in the position time series. The first few PCs often represent the biggest contributors to the variance of the network residual time series and the higher-order PCs are related to local site effects (Tiampo et al., 2012). Here we decompose the MSBAS time series for Campi Flegrei into the dominant eigenmodes that describe the local source physics.

We perform two separate analyses. The first is a covariance PCA decomposition of the east-west MSBAS displacement time series and the second is the same analysis on the vertical MSBAS displacement time series. The matrix \mathbf{T} consists of the MSBAS time series for each pixel in the

region shown in Figure 1, or 5308 locations. Each time series consists of 385 time steps, and the resulting covariance matrix, $S(x_i, x_j)$, has dimension 5308 x 5308.

The significant eigenmodes normally are selected by examination of the eigenvalue distribution, shown in Figure 4 (Preisendorfer, 1988; Tiampo et al., 2010). The first three eigenvalue, λ_j , account for approximately 98% of the variance in the vertical time series and 95% of the east-west time series. As a result, the first three EOFs are selected for further analysis.

FIGURE4

Figure 5 shows the first three EOFs and the associated PCA time series for the MSBAS vertical displacement time series. Note that the spatial eigenmodes, EOF1, EOF2 and EOF3, represent the amplitude of the signal that is accounted for at each point. The value at each location is then multiplied by the associated PCA time series in order to derive the actual time history attributed to each eigenmode at each location (Equation 2, above). In general, blue pixels are correlated with each other and anticorrelated with red pixels.

FIGURE5

EOF1 (Figure 5a) appears to be directly related to the central source expected to lie below the caldera and the associated PCA time series (Figure 5b) is similar to that for the original MSBAS time series of Figure 2. PCA2 (Figure 5d) shows a predominant linear trend that appears to represent the relationship between the Solfatara hydrothermal activity and a longer wavelength signal encompassing the larger caldera footprint (Figure 5c). EOF3 (Figure 5e) also presents a longer wavelength signal, potentially related to tropospheric error not corrected in the analysis. The associated PCA time series (Figure 5f) is noisy and supports the conclusion that the two

earlier modes account for most of the signal in the data, despite the fact that the third mode might be considered significant from Figure 4.

Figure 6 shows the first three EOFs and the associated PCA time series for the MSBAS east-west displacement time series. Note that these three eigenmodes do not necessarily represent the same activity seen in those recovered for the vertical displacements (Figure 5). However, the time series in PCA1 (Figure 6b) corresponds closely to that of the first time series in Figure 5, once the opposite signs are taken into account, suggesting a similar source process. Again, the deformation pattern in EOF1 (Figure 6a) is similar to that expected from a volcanic source located directly below the caldera. EOF2 and EOF3 (Figure 6c and Figure 6e) are less conclusive. Figure 6f is likely a correction to Figure 6d. However, the relatively sudden onset of new signal in 1997 suggests that some portion of the signal is related to the volcanic activity itself.

FIGURE6

EOF3 (Figure 6e) has a similar, but not identical pattern to that seen in EOF2. The strong signal seen on the western peninsula is likely a result of tropospheric noise. In addition, we again observe a strong signal in 1997 in PCA3 (Figure 6f), a pulse of activity that tapers off but remains observable through 2013. It should be noted that an EOF analysis is a linear decomposition of what are inherently nonlinear processes (Preisendorfer, 1988). The result is often a mixture of signals, particularly in the lower, shorter wavelength signals.

Figure 7 shows the vertical time series at the three locations shown by green triangles in Figure 3, obtained by summing EOF1, EOF2 and EOF3 in consecutive order (Equation 2, above). As expected, the vertical displacement at location c is very similar to that seen in Figure 2c.

However, location **b**, closer to the anticipated location of the central source is dominated by the linear subsidence that initiated in 2007. That signal dies away at location **a** and it appears to be dominated by the secondary uplift signal again associated with the primary source below the volcano.

FIGURE7

Given that we observe what appears to be only two separately resolvable signals in the PCA results, we inverted for two separate sources below the caldera, using a GA inversion technique and simple pressure sources.

5. GA Inversion

In order to invert for the various combinations of the three PCA modes shown above, we employed a GA inversion technique as outlined in Tiampo et al. (2004). Briefly, geophysical inverse problems generally involve employing large quantities of measured data, in conjunction with an efficient computational algorithm that explores the model space to find the global minimum associated with the optimal model parameters. In a GA, the parameters to be inverted for are coded as genes, and a large population of potential solutions for these genes is searched for the optimal solution. The basic structure of the GA code used here is modified from Michalewicz (1992). The process begins by representing the model to be optimized as a real-value string. Starting with an initial range of models, these algorithms progressively modify the solution by incorporating the evolutionary behavior of biological systems. The fitness of each solution is measured by a quantitative, objective function, the fitness function, FV. Next, the fittest members of each population are combined using probabilistic transition rules to form a new offspring population. Copying strings according to their fitness values means that strings

with a better value of fitness have a higher probability of contributing one or more offspring in the next generation. This procedure is repeated through a large number of generations until the best solution is obtained, based on the fitness measure (Michalewicz, 1992). Those members of the population with a fitness value greater than the average fitness of the population will increase in number exponentially, accelerating the convergence of the inversion process (Holland, 1975; Goldberg, 1989).

In this study we employ the GA to invert only for the vertical displacements for two respective time periods, 1993-1997 (subsidence) and 2007-2013 (uplift), using combinations of EOF1, EOF2 and EOF3 from Figures 5 and 6. A GA inversion can be very time consuming, particularly given the large number of points available in the DInSAR analysis. As a result, the vertical deformation alone was selected for the inversion. Given the high quality of the vertical deformation from the DInSAR analysis, it was sufficient for the inversion process alone. In addition, there was no independent data set such as local continuous GPS available to use as an independent check on the model, we did not include the east-west data in the inversion. That allowed us to use the east-west deformation as independent confirmation of the model quality. We assume that the source models are a combination of either one or two simple Mogi pressure sources with either positive or negative pressures for both time periods. Here the vertical and radial components of displacement in a half-space are defined as:

$$U_z = \frac{3\Delta V d}{4\pi R^{3/2}} \quad (3)$$

and

$$U_r = \frac{3\Delta V r}{4\pi R^{3/2}}. \quad (4)$$

Here U_z and U_r are the vertical and radial displacement, respectively, d is the depth to the source, R is the radial distance to a point on the surface, and ΔV is the change in volume of the source, here converted to the change in radius, r (Mogi, 1958).

6. Results

The GA inversion solved for the x and y location of each source, in UTM coordinates, the radius of the spherical pressure source, r , and the depth to each sphere, d . The initial search range of parameters for the GA was the spatial extent of the original InSAR images (Figure 2), r values between 20 and 200 m, and depths, d , of 1000 to 14000 m below the surface.

The inversion results for six different cases are shown in Table 2. The first case inverts EOF1 alone for the time period 2007-2013 for one positive source, two positive sources and two sources, one of which is negative and another which is positive. The second case inverts for EOF1 alone for the time period 1993-1999 for one negative source, two negative sources and two sources, one of which is negative and another which is positive. The third case inverts the sum of EOF1 and EOF2, 2007-2013, for the same three different source options as in Case 1. The fourth case inverts the sum of EOF1 and EOF2, 1993-1999, for the same three different source options as in Case 2. The fifth case inverts the sum of EOF1, EOF2 and EOF3, 2007-2013, for the same three different source options as in Case 1. The sixth case inverts the sum of EOF1, EOF2 and EOF3, 1993-1999, for the same three different source options as in Case 2. It should be noted that a number of other configurations, both for individual and summed EOF modes and for different source types, were tested as well, but none provided better solutions than those presented in Table 2.

Table 2 shows the time periods chosen for inversion analysis and the resulting parameters for the associated inflation or deflation (x and y location, d and ΔV). Also provided are the root-mean-

408 square (RMS) between the forward model produced by the best solution for each case and the
409 actual data seen in Figure 3, and the associated reduced chi-square value. Here the RMS value is
410 estimated using the error values for each of the 5308 locations provided in the Supplementary
411 Material of Samsonov et al. (2014b).

412 The results shown in Table 2 demonstrate that the addition of a second source of the same
413 polarity to the inversion does not improve the RMS. In each of those cases, the GA attempts to
414 minimize the size of that second source while either moving it to the same location as the first
415 source or as deep as possible in the medium. On the other hand, the addition of a second source
416 of opposite polarity always significantly improves the RMS of the solution.

417 Table 2 also shows that the RMS significantly improves with the addition of both EOF2 and
418 EOF3 to EOF1. The best solution for the 2007-2003 time period uses the sum of modes EOF1,
419 EOF2 and EOF3 and results in a shallower, positive source at approximately 3400 m in depth
420 and deeper, negative source at approximately 7624 m in depth. The best solution for the 1993-
421 1999 time period uses the sum of modes EOF1, EOF2 and EOF3 and results in a shallower,
422 negative source at approximately 2750 m in depth and deeper, negative source at approximately
423 8014 m in depth.

424 Figures 8 through 13 present the modelled results and residuals for the six different cases. We
425 omitted results for two sources with the same polarity because of the lack of increase in fitness
426 associated with those solutions. Figure 8 shows the forward model and residuals for the 1993-
427 1999 inversion of EOF1 alone, with both one negative source (Figures 8a and 8b) and for two
428 sources of opposite polarity (Figures 8c and 8d). The residuals are calculated as the difference
429 between the forward model from the best fit inversion for that decomposition and the original
430 MSBAS results for that time period. Figure 9 is for the same time period, 1993-1999, and the

same two cases, one source (Figures 9a and 9b) and two sources (Figures 9c and 9d). However, here the forward model is the result of the inversion of the summation of PCA modes EOF1 and EOF2. Figure 10 also represents the 1993-1999 time period and the same two cases, but the forward model is the result of the inversion of the summation of modes EOF1, EOF2 and EOF3. Note that the addition of EOF3 relocates the second source from the north of the caldera to south, similar to the results of Amoruso et al. (2015).

FIGURE8

FIGURE9

FIGURE10

Figure 11 presents the forward model results residuals for the 2007-2013 inversion of EOF1 alone, with both one positive source (Figures 11a and 11b) and for two sources of opposite polarity (Figures 11c and 11d). Figure 12 also shows the results for the 2007-2013 time period and the same two cases, but here the forward model is the result of the inversion of the summation of modes EOF1 and EOF2. Figure 13 also represents the period 2007-2013 and the same two cases, but here the forward model is the result of the inversion of the summation of modes EOF1, EOF2 and EOF3. Here all three inversions place the second source in the south of the caldera. The final model suggests that both sources are further south than expected and minimize the residuals from the Solfatara region.

FIGURE11

FIGURE12

FIGURE13

Displacements in the east-west direction were modeled in order to assess how well the source models agreed with the complete displacement field. Figure 14 presents the results from the inversion of the summation of modes EOF1, EOF2 and EOF3 for both time periods. Figure 14a shows the modelled east-west displacements for the two source model derived for 1993-1999, as given in Figure 10. Figure 14b shows the residuals between the model of Figure 14a and the actual displacements. Figure 14c are the modelled east-west displacements for the two source model of Figure 13, the time period 2007-2013. Figure 14d presents the residuals between model shown in Figure 14c and actual the displacements. The results for both models are in good agreement with the actual data, although the displacements associated with the subsidence model (Figures 14a and 14b), 1993-1999, suggest that the modeled displacements are slightly underfit by the model. The wavelength of the residual signal suggests that is the difference is contained in the shallow source.

FIGURE 14

7. Conclusions

In this work we applied, for the first time, a PCA decomposition analysis to the advanced MSBAS DInSAR time series of ground deformation in the Campi Flegrei caldera. The MSBAS time series incorporate ERS-1/2, ENVISAT and RADARSAT-2 data and result in nearly twenty years of data, with uninterrupted temporal coverage for 2003-2013. The PCA analysis produces three significant eigenmodes for both the vertical and east-west time series. These time series were inverted using a GA technique for simple Mogi pressure sources and a variety of cases. The fit to the actual data increases progressively with the addition of each mode, suggesting that each contains important information related to the source mechanisms. The best fit occurs for an inversion that sums all three modes (EOF1, EOF2 and EOF3) and for two sources with opposite

477 polarity, for both the period of subsidence (1993-1999) and the period of uplift (2007-2013). In
478 the first case, a shallower source is deflating while a deeper source inflates; in the second case, a
479 shallower source is inflating while the deeper source deflates. The time series for EOF2 and
480 EOF3 suggest that a sharp pulse in activity occurred between 1997 and 2002, potentially
481 indicating that the dynamics of the system changed significantly. This hypothesis is supported
482 by a similar uplift signal seen in levelling data from Amoruso et al. (2014a), at the same time that
483 the CO₂/H₂O ratio in local fumaroles starts to increase, potentially as a result of an increased
484 contribution of the magmatic component (Chiodini et al., 2012). It has been suggested that this
485 change was driven by magma fed from a deeper magma chamber, such as that found in our
486 inversion for the sum of modes EOF1, EOF2 and EOF3 (Zollo et al., 2008; Amoruso et al.,
487 2014a; Di Vito et al., 2016). Incorporation of all three modes is necessary to significantly
488 improve the fit and model the two sources together.

489 Past work, using various combinations of geodetic data, including leveling, trilateration, GPS,
490 gravity and DInSAR, have found that the shallower source can be fit better using different
491 geometries and some combination of shallower hydrothermal sources (see, e.g. De Natale et al.
492 1991; Battaglia et al., 2006; De Natale et al., 2006; Gottsmann et al., 2005, 2006; Amoruso et al.,
493 2008; Chiodini et al., 2010; Camacho et al., 2011; Trasatti et al., 2011; Chiodini et al., 2012;
494 Amoruso et al., 2014a,b; Samsonov et al., 2014b; Trasatti et al., 2015; Di Vito et al., 2016).

495 Here we found that two simple, spherical sources of opposite polarity, one deeper and the second
496 shallow, provided an adequate fit to the data without resorting to sills or spheroidal magma
497 chambers.

498 The final models for both periods place the shallower source at between 2750 and 3400 m below
499 the caldera, at either the upper or lower edge of the gas bearing rock layer (Figure 1). The

deeper source is more stable, at 7600 to 8000 meters in depth, also as suggested by earlier work (Trasatti et al., 2011, 2015). Expansion of the existing SAR data set using new satellite data (e.g. Sentinel-1a and 1b) will help to better characterize these sources with time. This study provides evidence for the effectiveness of PCA in denoising large geophysical data sets, including DInSAR data. Dense time series are critical to the process and, as a result, suggests that MSBAS time series will be of increasing importance in the accurate and reliable estimation of natural and anthropogenic hazards.

Acknowledgements

We thank the Canadian Space Agency for providing RADARSAT-2 data and the European Space Agency for providing ERS and ENVISAT. We also would like to thank three anonymous reviewers for their thorough reviews. Figures were plotted with GMT. The work of PG was supported by a Banting Postdoctoral Fellowship. The work of KFT was supported by an NSERC Discovery Grant and CIRES, University of Colorado Boulder. This work also was supported by the AQUARISK Spanish project and the EU MED-SUV project.

- 518 Anghel, M., Y. Ben-Zion, and R.R. Martinez (2004), Dynamical system analysis and forecasting
 519 of deformation produced by an earthquake fault, *Pure and Applied Geophysics*, 161,
 520 doi:10.1007/s00024-004-2547-9.
- 521 Amoruso, A., Crescentini, L., Berrino, G. (2008), Simultaneous inversion of deformation and
 522 gravity changes in a horizontally layered halfspace: Evidences for magma intrusion during the
 523 1982–1984 unrest at Campi Flegrei caldera (Italy), *Earth Planet. Sci. Lett.*, 272,
 524 doi:10.1016/j.epsl.2008.04.040.
- 525 Amoruso, A., Crescentini, L., and Sabetta, I. (2014a), Paired deformation sources of the Campi
 526 Flegrei caldera (Italy) required by recent (1980-2010) deformation history, *J. Geophys. Res.*, 119,
 527 858–879, doi:10.1002/2013JB010392.
- 528 Amoruso, A., L. Crescentini, I. Sabetta, P. De Martino, F. Obrizzo, and U. Tammaro (2014b),
 529 Clues to the cause of the 2011–2013 Campi Flegrei caldera unrest, Italy, from cGPS data,
 530 *Geophys. Res. Lett.*, 41, 3081–3088, doi:10.1002/2014GL059539.
- 531 Amoruso, A., L. Crescentini, R. Scarpa, R. Bilham, A. T. Linde, and I. S. Sacks (2015), Abrupt
 532 magma chamber contraction and microseismicity at Campi Flegrei, Italy: Cause and effect
 533 determined from strainmeters and tiltmeters, *J. Geophys. Res.*, 120, 5467–5478,
 534 doi:10.1002/2015JB012085.
- 535 Arienzo, I., Moretti, R., Civietta, L., Orsi, G., and Papale, P. (2010), The feeding system of
 536 Agnano-Monte Spina eruption (Campi Flegrei, Italy): Dragging the past into present activity and
 537 future scenarios, *Chemical Geology*, 270, 135-147.
- 538 Aubrey, D. G., and K. O. Emery, (1983), Eigenanalysis of recent United States sea levels, *Cont.*
 539 *Shelf Res.*, 2, 21– 33, 1983.
- 540 Battaglia, M., C. Troise, F. Obrizzo, F. Pingue, and G. De Natale (2006), Evidence for fluid
 541 migration as the source of deformation at Campi Flegrei Caldera (Italy), *Geophys. Res. Lett.*, 33,
 542 L01307, doi:10.1029/2005GL024904.
- 543 Berardino, P., Fornaro, G., and Lanari, R. (2002), A new algorithm for surface deformation
 544 monitoring based on small baseline differential SAR interferograms. *IEEE Trans. Geosc. Rem.*
 545 *Sens.*, 40, 2375-2383.
- 546 Bonafede, M. and Mazzanti, M., (1998), Modelling gravity variations consistent with ground
 547 deformation in the Campi Flegrei caldera (Italy), *J. Volc. Geotherm. Res.*, 81:137–157.
- 548 Caliro, S., Chiodini, G., Moretti, R., Avino, R., Granieri, D., Russo, M., Fiebig, J. (2007). The
 549 origin of the fumaroles of La Solfatara (Campi Flegrei, South Italy), *Geochim. Cosmochim. Acta*,
 550 71: 3040-3055.
- 551 Camacho, A.G., González, P.J., Fernández, J., Berrino, G. (2011), Simultaneous inversión of
 552 Surface deformation and gravity changes by means of extended bodies with a free geometry:
 553 Application to deforming calderas, *J. Geophys. Res.*, 116, B10401, doi: 10.129/2010JB008165.
- 554 Chaussard, E., R. Bürgmann, M. Shirzaei, E. J. Fielding, and B. Baker (2014), Predictability of
 555 hydraulic head change and characterization of aquifer-system and fault properties from InSAR-
 556 derived ground deformation, *J. Geophys. Res.*, 119, doi:10.1002/2014JB011266.
- 557 Chiarabba, C., Moretti, M. (2006), An insight into the unrest phenomena at the Campi Flegrei
 558 caldera from Vp and Vp/Vs tomography, *Terra Nova*, 18, doi:10.1111/j.1365-
 559 3121.2006.00701.x.
- 560 Chiodini, G., Caliro, S., Cardellini, C., Granieri, D., Avino, R., Baldini, A., Donnini, M.,
 561 Minopoli, C. (2010), Long-term variations of the Campi Flegrei, Italy, volcanic system as

revealed by the monitoring of hydrothermal activity, *J. Geophys. Res.*, 115, B03205, doi:10.1029/2008JB006258.

Chiodini, G., S. Caliro, P. De Martino, R. Avino, and F. Gherardi (2012), Early signals of new volcanic unrest at Campi Flegrei caldera? Insights from geochemical data and physical simulations, *Geology*, 40, doi:10.1130/G33251.1.

D'Auria, L., Giudicepietro, F., Martini, M. and Lanari, R. (2012), The 4D imaging of the source of ground deformation at Campi Flegrei caldera (southern Italy), *J. of Geophys. Res.* 117, B08209, doi:10.1029/2012JB009181.

D'Auria, L., Giudicepietro, F., Aquino, I., Borriello, G., Del Gaudio, C., Lo Bascio, D., Martini, M., Ricciardi, G.P., Ricciolino, P., and Ricco, C. (2011), Repeated fluid-transfer episodes as a mechanism for the recent dynamics of Campi Flegrei caldera (1989–2010), *J. of Geophys. Res.* 116, B04313, doi:10.1029/2010JB007837.

D'Auria, L., Pepe, S., Castaldo, R., Giudicepietro, F., Macedonio, G., Ricciolino, P., Tizzani, P., Casu, F., Lanari, R., Manzo, M., Martini, M., Sansosti, E., Zinno, I. (2015), Magma injection beneath the urban area of Naples: a new mechanism for the 2012-2013 volcanic unrest at Campi Flegrei caldera, *Scientific Reports*, doi:10.1038/srep13100.

Del Gaudio, C., Aquino I., Ricciardi, G.P., Ricco, C., Scandone, R. (2010), Unrest episodes at Campi Flegrei: A reconstruction of vertical ground movements during 1905-2009, *J. Volc. Geoth. Res.*, 195, doi:10.1016/j.jvolgeores.2010.05.014.

De Martino, P., U. Tammaro, F. Obrizzo (2014), GPS time series at Campi Flegrei caldera (2000–2013), *Ann. Geophys.*, 57(2), S0213, doi:10.4401/ag-6431.

De Natale, G., F. Pingue, P. Allard, and A. Zollo (1991), Geophysical and geochemical modelling of the 1982–1984 unrest phenomena at Campi Flegrei caldera (southern Italy), *J. Volcanol. Geotherm. Res.*, 48, 199–222.

De Natale, G., Troise, C., Pingue, F., Mastrolorenzo G., Pappalardo L., Battaglia M., and Boschi E. (2006), The Campi Flegrei caldera: unrest mechanisms and hazards, in Troise C., De Natale G. & Kilburn C.R.J. *Mechanisms of activity and unrest at large calderas*. Geological Society, London, Special Publications, 269:25-45, doi:10.1144/GSL.SP.2006.269.01.03.

De Siena, L., E. Del Pezzo, and F. Bianco (2010), Seismic attenuation imaging of Campi Flegrei: Evidence of gas reservoirs, hydrothermal basins, and feeding systems, *J. Geophys. Res.*, 115, B09312, doi:10.1029/2009JB006938.

Di Vito, M.A., Acocella, V., Aiello, G., Barra, D., Battaglia, M., Carandente, A., Del Gaudio, C., de Vita, S., Ricciardi, G.P., Ricco, C., Scandone, R., and Terrasi, F. (2016), Magma transfer at Campi Flegrei caldera (Italy) before the 1538 AD eruption, *Scientific Reports*, doi:10.1038/srep32245.

Dong, D., Fang, P., Bock, Y., Webb, F., Prawirodirdjo, L., Kedar, S., Jamason, P. (2006), Spatiotemporal filtering using principal component analysis and Karhunen-Loeve expansion approaches for regional GPS network analysis, *J. Geophys. Res.*, 111, B03405, doi:10.1029/2005JB003806.

Dvorak, J.J. and Berrino, G., 1991. Recent ground movements and seismic activity in Campi Flegrei, southern Italy: episodic growth of a resurgent dome, *J. Geophys. Res.*, 96:2309–2323.

Farr, T., and Kobrick, M. (2000), Shuttle Radar Topography Mission produces a wealth of data, *EOS Transactions, AGU*, 81:583–585.

Fernández, J., Tizzani, P., Manzo, M., Borgia, A., González, P.J., Martí, J., Pepe, A., Camacho, A.G., Casu, F., Berardino, P., Prieto, J.F., Lanari, R. (2009). Gravity-driven deformation of

Tenerife measured by InSAR time series analysis, *Geophys. Res. Lett.*, 36, L04306, doi: 10.1029/2008GL036920.

Fernández, J., Tiampo, K.F. and Rundle, J.B., 2001. Viscoelastic displacement and gravity changes due to point magmatic intrusions in a gravitational layered solid Earth, *Geophys. J. Int.*, 146:155–170.

Ferretti, A., Prati, C., Rocca, F. (2001), Permanent scatterers in SAR interferometry. *IEEE Trans. Geosc. Rem. Sens.*, 39, 8-20.

Fukunaga, K. (1970), Introduction to Statistical Pattern Recognition, Academic, San Diego, Calif.

Goldberg, D.E. (1989), Genetic Algorithms in Search, Optimization, and Machine Learning (Addison Wesley, Reading, MA).

Gottsmann, J., Camacho, A., Fernández, J., and Tiampo, K.F. (2006), Spatio-temporal variations in vertical gravity gradients at the Campi Flegrei volcano (Italy): A case for source multiplicity during unrest? *Geophysical Journal International*, 167, doi:10.1111/j.1365-246X.2006.03157.x, 1089-1096.

Gottsmann, J., Folch, A. & Rymer, H. (2005), Unrest at Campi Flegrei: a contribution to the magmatic vs. hydrothermal debate from inverse and finite element modeling, *J. Geophys. Res.*, 111, B07203, doi:10.1029/2005JB003745.

Holland, J.H. (1975), Adaptation in Natural and Artificial Systems (MIT Press, Cambridge, MA).

Holmes, P., J. L. Lumley, and G. Berkooz, (1996), Turbulence, Coherent Structures, Dynamical Systems and Symmetry, Cambridge Univ. Press, New York.

Hotelling, H. (1933), Analysis of a complex of statistical variables into principal components, *J. Educ. Psych.*, 24, 417– 520.

Hooper, A. (2008), A multi-temporal InSAR method incorporating both persistent scatterer and small baseline approaches. *Geophysical Research Letters*, 35:16302.

Isaia, R., Marianelli, P., Sbrana, A. (2009), Caldera unrest prior intense volcanism in Campi Flegrei (Italy) at 4.0 ka B.P.: Implications for caldera dynamics and future eruptive scenarios, *Geophysical Research Letters*, 36:L21303.

Lipovsky, B. (2011), Physical and statistical models in deformation geodesy, MS thesis, UC Riverside: Geological Sciences. [Available at <http://escholarship.org/uc/item/4mv4f384>.]

Main, I.G., L. Li, K. J. Heffer, O. Papasouliotis, and T. Leonard (2006), Long-range, critical-point dynamics in oil field flow rate data, *Geophys. Res. Lett.*, 33, L18308, doi:10.1029/2006GL027357.

Masterlark, T. (2007), Magma intrusion and deformation predictions: Sensitivities to the Mogi assumptions, *J. Geophys. Res.*, 112, B06419, doi:10.1029/2006JB004860.

Michalewicz, Z. (1992), Genetic Algorithms + Data Structures = Evolution Programs. Springer-Verlag, New York, NY.

Moghaddam, B., W. Wahid, and A. Pentland, Beyond eigenfaces: Probabilistic matching for face recognition, paper presented at *Third IEEE International Conference on Automatic Face and Gesture Recognition*, Nara, Japan, 14– 16 April 1998.

Mogi, K. (1958), Relations between the eruptions of various volcanoes and the deformations of the ground surfaces around them, *Bull. Earth. Res. Inst. Tokyo*, 36, 99-134.

Moretti, R., Arienzo, I., Civetta, L., Orsi, G., Papale, P. (2013), Multiple magma degassing sources at an explosive volcano, *Earth Plan. Sci. Lett.*, 367: 95-104.

652 Mormone, A., Piochi, M., Belltreccia, F., De Astis, G., Moretti, R., Della Ventura, G., Cavallo,
 653 A., Mangiacapra, A. (2011), A CO₂-rich magma source beneath the Phlegraean Volcanic
 654 District (Southern Italy): Evidence from a melt inclusion study, *Chemical Geology*, 287:66-80.
 655 Orsi, G., Di Vito, M.A., Isaia, R. (2004), Volcanic hazard assessment at the restless Campi
 656 Flegrei caldera. *Bull. Volc.* 66, 514–530.
 657 Penland, C. (1989), Random forcing and forecasting using principal oscillation pattern analysis,
 658 *Mon. Weather Rev.*, 117, 2165 – 2185.
 659 Penland, C., and P. D. Sardeshmukh (1995), The optimal growth of tropical sea surface
 660 temperature anomalies, *J. Clim.*, 8, 1999 - 2024.
 661 Posadas, A.M., F. Vidal, F. DeMiguel, G. Alguacil, J. Pena, J.M. Ibanez, and J. Morales (1993),
 662 Spatial-temporal analysis of a seismic series using the principal components method – the
 663 Antequera series, Spain, 1989, *J. Geophys. Res.*, 98, 1923-1932.
 664 Preisendorfer, R. W. (1988), Principle Component Analysis in Meteorology and Oceanography,
 665 Elsevier Sci., New York.
 666 Press, W. H., B. P. Flannery, S. A. Teukolsky, and W. T. Vetterling, (1992), Numerical Recipes
 667 in C, 2nd ed., Cambridge Univ. Press, New York.
 668 Remy, D., J. L. Froger, H. Perfettini, S. Bonvalot, G. Gabalda, F. Albino, V. Cayol, D. Legrand,
 669 and M. Saint Blanquat (2014), Persistent uplift of the Lazufre volcanic complex (Central Andes):
 670 New insights from PCAIM inversion of InSAR time series and GPS data, *Geochem. Geophys.*
 671 *Geosyst.*, 15, 3591–3611, doi:10.1002/2014GC005370.
 672 Rudolph, M. L., M. Shirzaei, M. Manga, and Y. Fukushima (2013), Evolution and future of the
 673 Lusi mud eruption inferred from ground deformation, *Geophys. Res. Lett.*, 40, 1089–1092,
 674 doi:10.1002/grl.50189.
 675 Rosen, P., Hensley, P., Joughin, I., Li, F., Madsen, S., Rodriguez, E., Goldstein, R. (2000),
 676 Synthetic aperture radar interferometry, *Proc. IEEE*, 88(3), 333–382.
 677 Rosi, M., A. Sbrana, C. Principe (1983), The Phlegraean Fields; structural evolution, volcanic
 678 history and eruptive mechanisms, *J. Volcanol. Geotherm. Res.*, 17, 273–288.
 679 Samsonov, S. and d'Oreye, N. (2012), Multidimensional time series analysis of ground
 680 deformation from multiple InSAR data sets applied to Virunga Volcanic Province, *Geophysical*
 681 *Journal International*, 191(3):1095-1108, doi:10.1111/j.1365-246X.2012.05669.x.
 682 Samsonov, S., d'Oreye, N., González, P., Tiampo, K., Ertolahti, L., Clague, J.J. (2014a), Rapidly
 683 accelerating subsidence in the Greater Vancouver region from two decades of ERS-ENVISAT-
 684 RADARSAT-2 DInSAR measurements, *Rem. Sens. Env.*, doi:10.1016/j.rse.2013.12.017.
 685 Samsonov, S., d'Oreye, N., and Smets, B. (2013), Ground deformation associated with post-
 686 mining activity at the French-German border revealed by novel InSAR time series method,
 687 *International Journal of Applied Earth Observation and Geoinformation*, 23,142-154.
 688 Samsonov, S.V., Tiampo, K.F., Camacho, A., Fernández, J., González, P.J. (2014b),
 689 Spatiotemporal analysis and interpretation of 1993-2013 ground deformation at Campi Flegrei,
 690 Italy, observed by advanced DInSAR, *Geophys. Res. Lett.*, doi:10.1002/2014GL061307.
 691 Samsonov, S., van der Kooij, M., K. Tiampo, (2011). A simultaneous inversion for deformation
 692 rates and topographic errors of DInSAR data utilizing linear least square inversion technique.
 693 *Computers and Geosciences*, 37:1083-1091.
 694 Savage, J. C. (1988), Principal component analysis of geodetically measured deformation in
 695 Long Valley caldera, eastern California, 1983 – 1987, *J. Geophys. Res.*, 93, 13,297 - 13,305.
 696 Small, D., and S. Islam (2007), Decadal variability in the frequency of fall precipitation over the
 697 United States, *Geophys. Res. Lett.*, 34, L02404, doi:10.1029/2006GL028610.

Smith, E.G.C., T.D. Williams, and D.J. Darby (2007), Principal component analysis and modeling of the subsidence of the shoreline of Lake Taupo, New Zealand, 1983–1999: Evidence for dewatering of a magmatic intrusion?, *J. Geophys. Res.*, 112, B08406, doi:10.1029/2006JB004652.

Tiampo, K., Fernández, J., Jentzsch, G., Charco, M., and J. Rundle, (2004), Inverting for the parameters of a volcanic source using a genetic algorithm and a model for magmatic intrusion in elastic-gravitational layered earth models. *Computers and Geosciences*, 30 (9), 985-1001.

Tiampo, K.F., Mazzotti, S., James, T. (2012), Analysis of GPS measurements in eastern Canada using principal component analysis, *Pure and Applied Geophysics*, doi:10.1007/s00024-011-0420-1.

Tiampo, K.F., Rundle, J.B., Gross, S.J., McGinnis, S., W. Klein (2002), Eigenpatterns in southern California seismicity, *J. Geophys. Res.*, 107, 2354, doi:10.1029/2001JB000562.

Tiampo, K.F., J.B. Rundle, W. Klein, Y. Ben-Zion, S. McGinnis, (2004), Using eigenpattern analysis to constrain seasonal signals in southern California, *Pure and Applied Geophysics*, 161: 1991. doi:10.1007/s00024-004-2545-y.

Trasatti, E., M. Bonafede, C. Ferrari, C. Giunchi, and G. Berrino (2011), On deformation sources in volcanic areas: Modeling the Campi Flegrei (Italy) 1982–84 unrest, *Earth Plan. Sci. Lett.*, 306, 175–185, doi:10.1016/j.epsl.2011.03.033.

Trasatti, E., M. Polcari, M. Bonafede, and S. Stramondo (2015), Geodetic constraints to the source mechanism of the 2011–2013 unrest at Campi Flegrei (Italy) caldera, *Geophys. Res. Lett.*, 42, 3847–3854, doi:10.1002/2015GL063621.

Troiano, A., M. G. Di Giuseppe, Z. Petrillo, C. Troise, and G. De Natale (2011), Ground deformation at calderas driven by fluid injection: Modelling unrest episodes at Campi Flegrei (Italy), *Geophys. J. Int.*, 187, 833–847, doi:10.1111/j.1365-246X.2011.05149.x.

Troise, C., De Natale, G., Pingue, F., Obrizzo, F., De Martino, P., Tammaro, U., Boschi, E., (2007). Renewed ground uplift at Campi Flegrei caldera (Italy): New insight on magmatic processes and forecast, *Geophysical Research Letters* 34, L03301. doi:10.1029/2006GL028545.

Usai, S. (2003), A least squares database approach for SAR interferometric data. *IEEE Trans. Geosc. Rem. Sens.*, 41:753760.

Vautard, R., and M. Ghil (1989), Singular spectrum analysis in nonlinear dynamics, with applications to paleodynamic time series, *Physica D*, 35, 395 - 424.

Wadge, G. (2003). A strategy for the observation of volcanism on Earth from space. *Phil. Trans. Royal Soc. Lond. A*, 361, 145-156.

Wegmuller, U. and Werner, C. (1997), Gamma SAR processor and interferometry software, in *Third ERS Symposium on Space at the service of our Environment*, Florence, Italy.

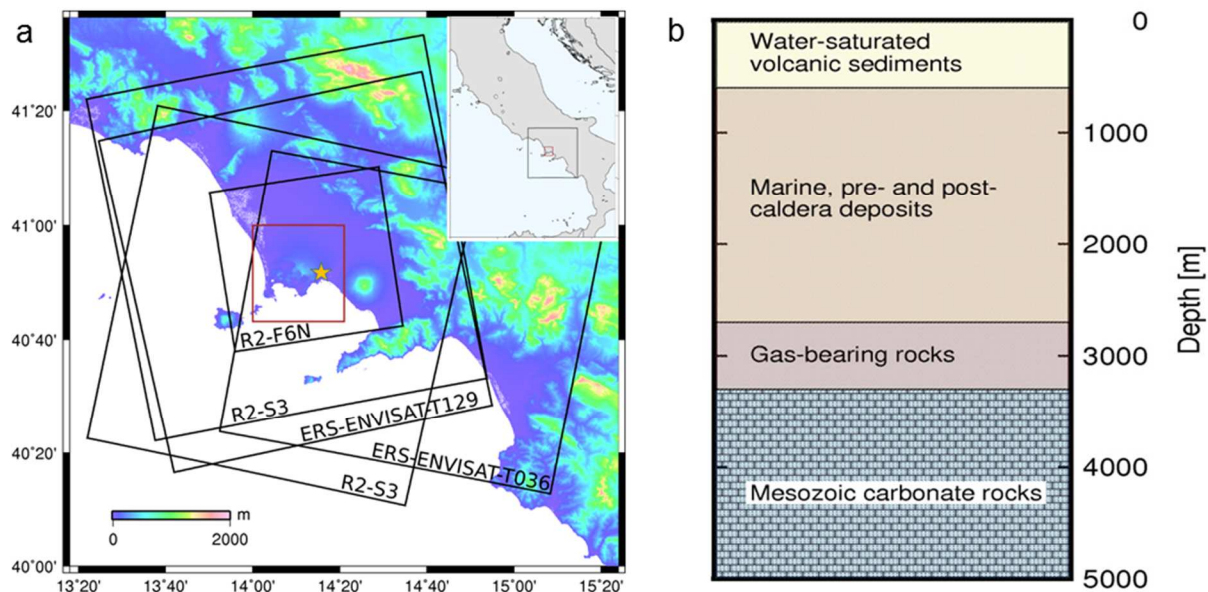
Wessel, P. and Smith, W. (1998), New, improved version of the generic mapping tools released, *EOS Transactions, AGU*, 79:579.

Zerbini, S., Raicich, F., Richter, B., Gorini, V., M. Errico (2010), Hydrological signals in height and gravity in northeastern Italy inferred from principal components analysis, *J. Geodynamics*, doi:10.1016/j.jog.2009.11.001.

Zollo, A., N. Maercklin, M. Vassallo, D. Dello Iacono, J. Virieux, and P. Gasparini (2008), Seismic reflections reveal a massive melt layer feeding Campi Flegrei caldera, *Geophys. Res. Lett.*, 35, L12306, doi:10.1029/2008GL034242.

742

743



744

745 **Figure 1:** (a) Map of the Naples region, Italy, with Campi Flegrei caldera outlined in the red box
 746 (city of Naples, orange star). Black boxes identify frames for each of the ERS-ENVISAT (T129
 747 and T036) and RADARSAT-2 (S3, both ascending and descending, and F6N) radar image
 748 frames. (b) Simplified geologic cross section of the caldera structure (modified from Samsonov
 749 et al. 2014b).

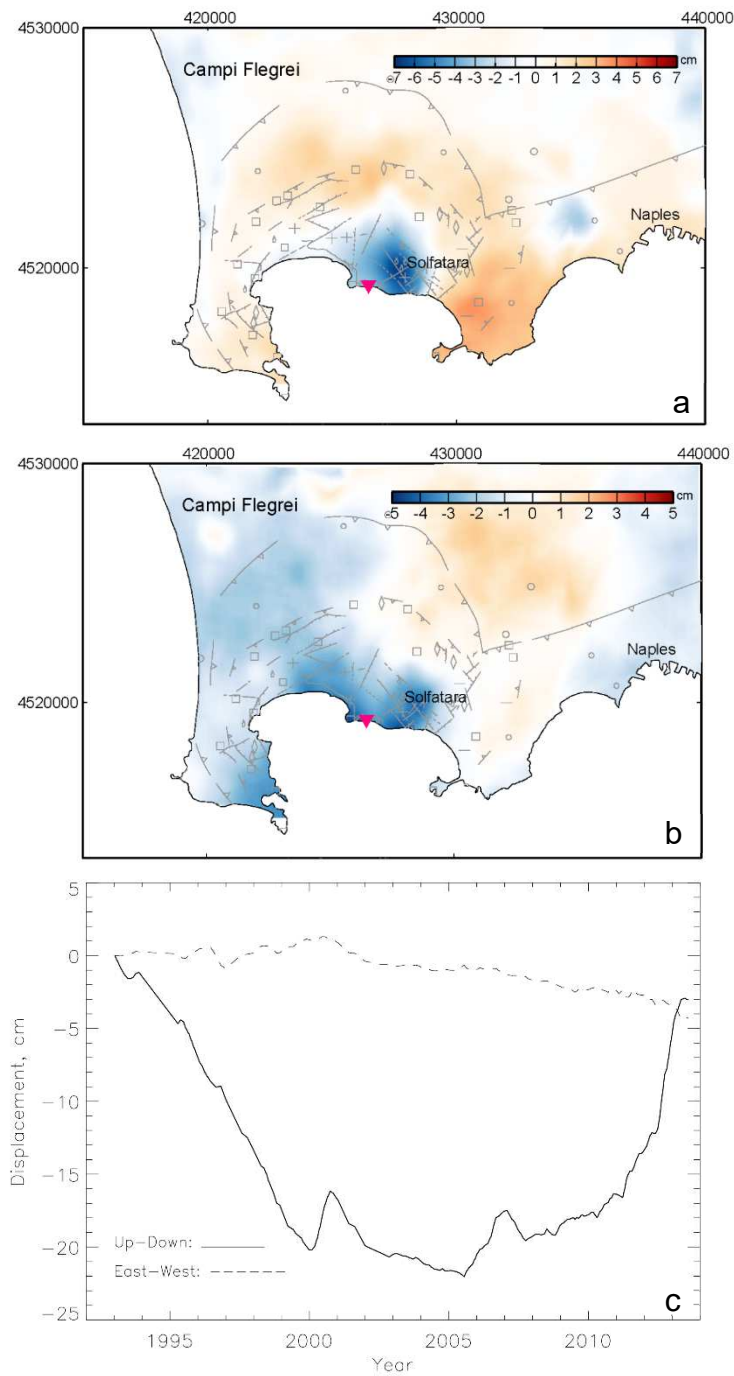


Figure 2: MSBAS results, 1992-2013, for the images outlined in Figure 1 (see Table 1 for details). a) Vertical component of deformation, 1992-2013; b) east-west component of deformation, 1992-2013; c) time series of vertical and east-west components identified in (a) and (b) by pink triangle (modified from Samsonov et al., 2014b).

a

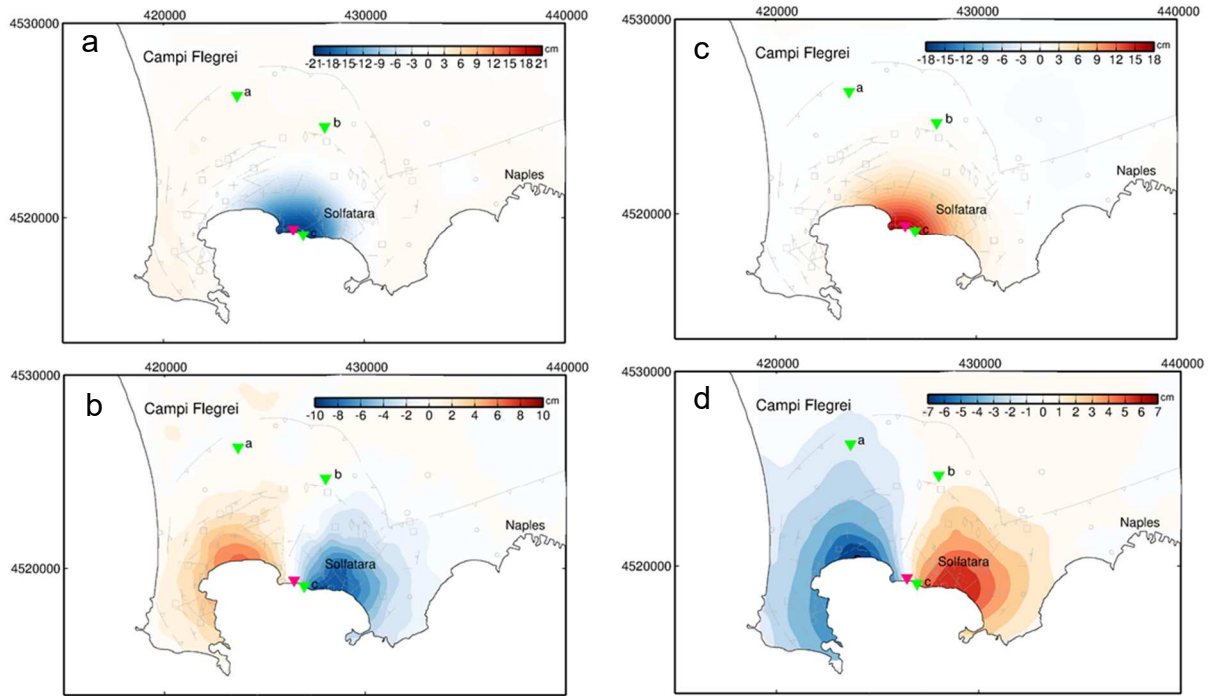


Figure 3: Net surface deformation for two time periods chosen from the time series of Figure 1. a) Vertical surface displacement, 1993-1999 and b) east-west surface displacement, 1993-1999. c) Vertical surface displacement, 2007-2013 and c) east-west surface displacement, 2007-2013. Pink triangle is as shown in Figure 2. Green triangles identify location of time series in Figure 7.

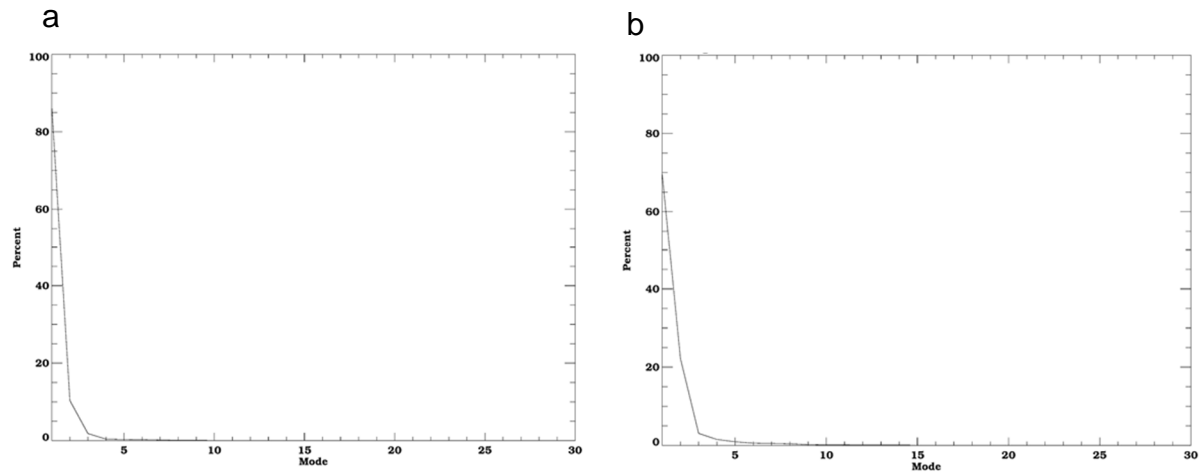
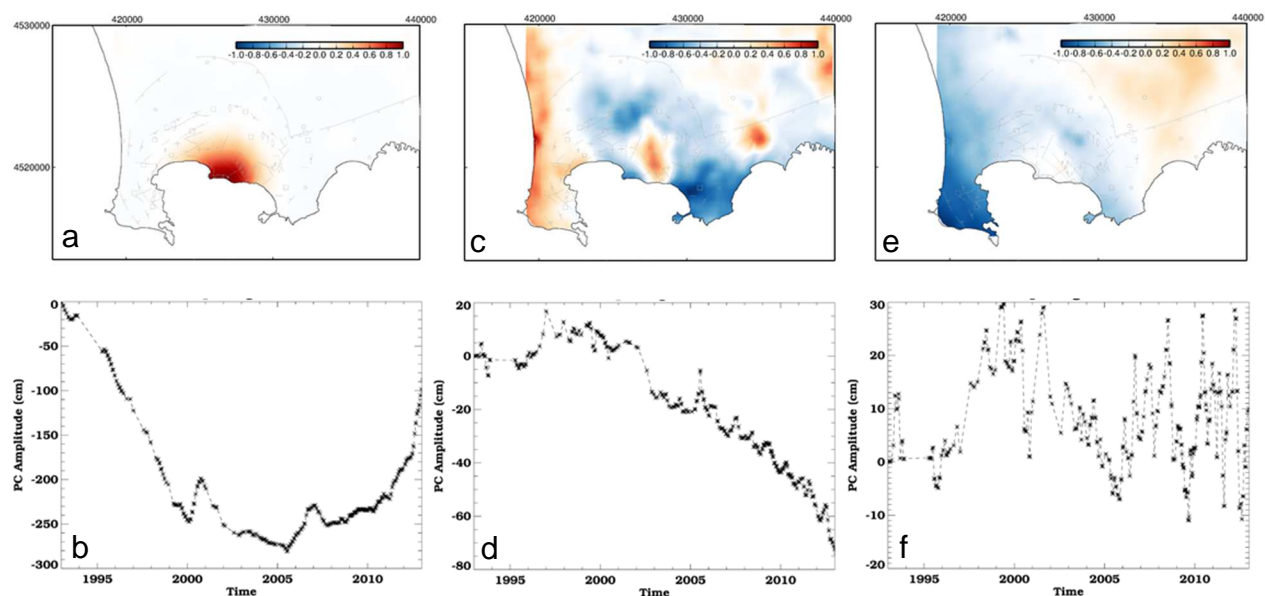


Figure 4: Eigenvalue plots showing the percentage of variance accounted for by each eigenvector mode for the decomposition of MSBAS time series of surface displacement in a) the vertical direction and b) the east-west direction. Note that the x-axis begins at one, not zero.



812

Figure 5: First three eigenmodes for vertical displacement, 1993-2013. a) First spatial eigenmode (EOF1); b) principal component time series associated with EOF1 (PCA1); c) second spatial eigenmode (EOF2); d) principal component time series associated with EOF2 (PCA2); e) third spatial eigenmode (EOF3); f) principal component time series associated with EOF3 (PCA3). Here blue is anticorrelated with red, EOF plots a, c, and e.

818

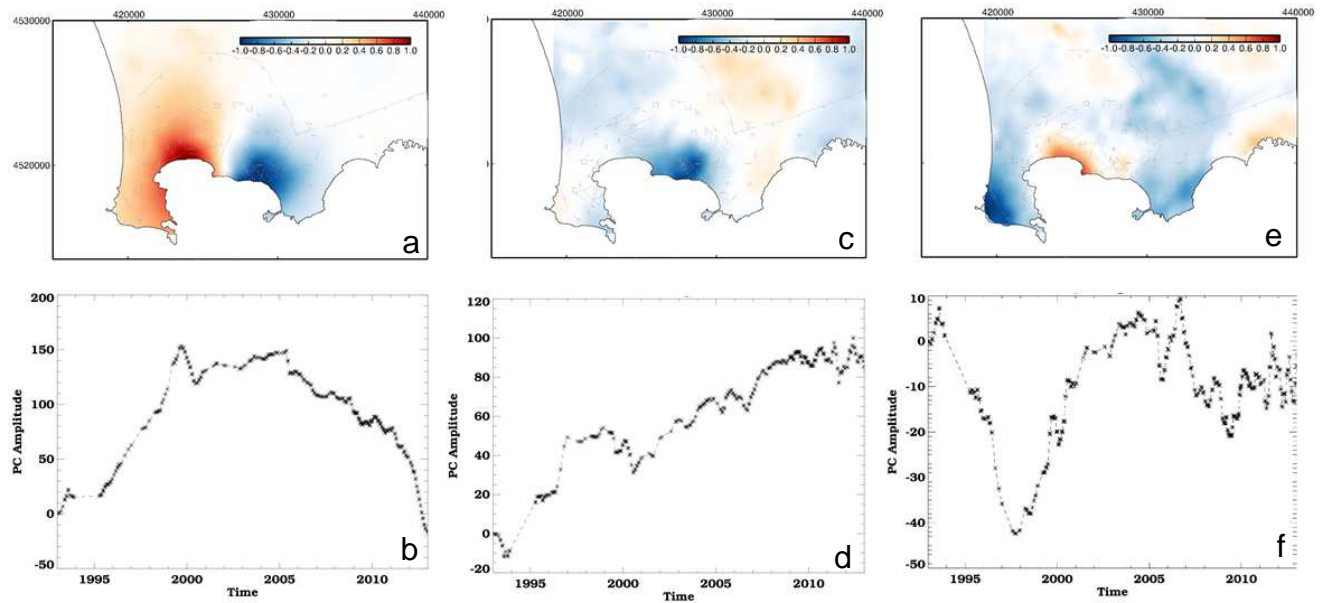
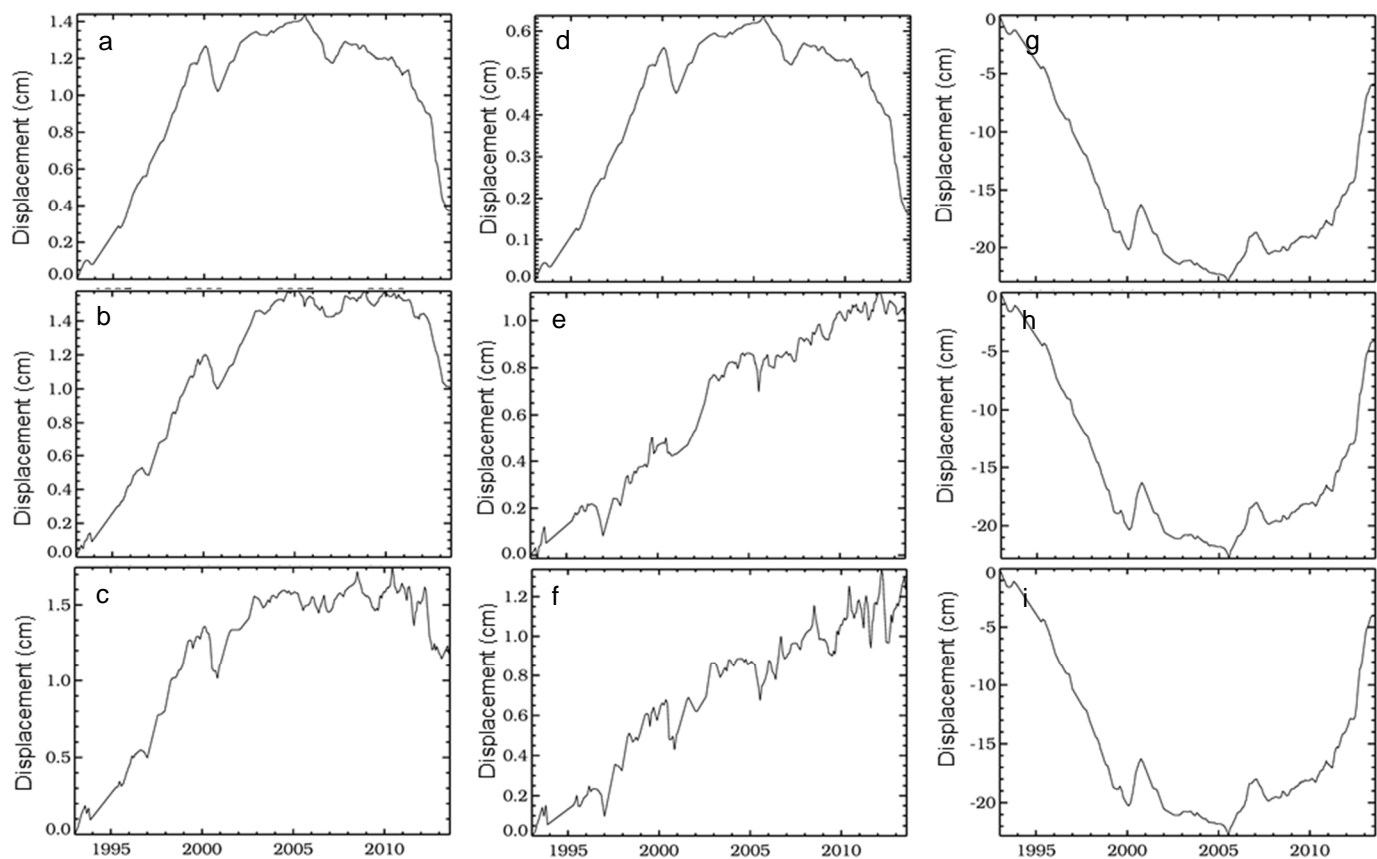
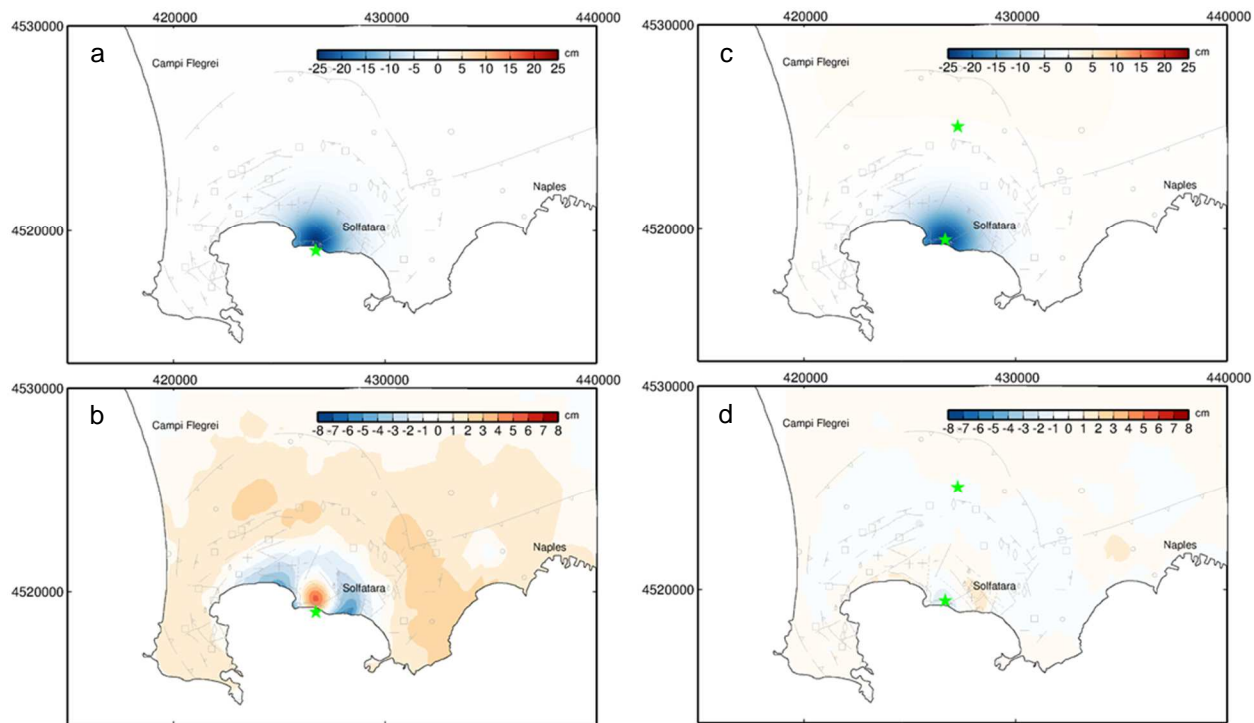


Figure 6: First three eigenmodes for east-west displacement, 1993-2013. a) First spatial eigenmode (EOF1); b) principal component time series associated with EOF1 (PCA1); c) second spatial eigenmode (EOF2); d) principal component time series associated with EOF2 (PCA2); e) third spatial eigenmode (EOF3); f) principal component time series associated with EOF3 (PCA3). Here blue is anticorrelated with red, EOF plots a, c, and e.



832 **Figure 7:** Time series of vertical displacement for combinations of the first three EOFs at the
833 locations shown by green triangles in Figure 3. Vertical displacement at location **a**, Figure 3, is
834 shown for a) EOF1, b) EOF1 and EOF2, summed, and c) EOF1, EOF2 and EOF3, summed.
835 Vertical displacement at location **b**, Figure 3, is shown for d) EOF1, e) EOF1 and EOF2,
836 summed, and f) EOF1, EOF2 and EOF3, summed. Vertical displacement at location **c**, Figure 3,
837 is shown for g) EOF1, h) EOF1 and EOF2, summed; and i) EOF1, EOF2 and EOF3, summed.

838
839
840
841



842 **Figure 8:** Modelled displacements and residuals in the vertical direction inverted for EOF1 for
843 the time period 1993-1999 (subsidence). a) Displacements for a single source model, location
844 shown by green star, at a depth of 1665 m; b) residuals between model shown in (a) and actual
845 displacements (Figure 2); c) displacements for a two source model, locations shown by green
846 stars, at depths of 2069 m (south, negative) and 13802 m (north, positive); d) residuals between
847 model shown in (c) and actual displacements (Figure 2). All displacements and residuals in cm;
848 source details are given in Table 2.
849

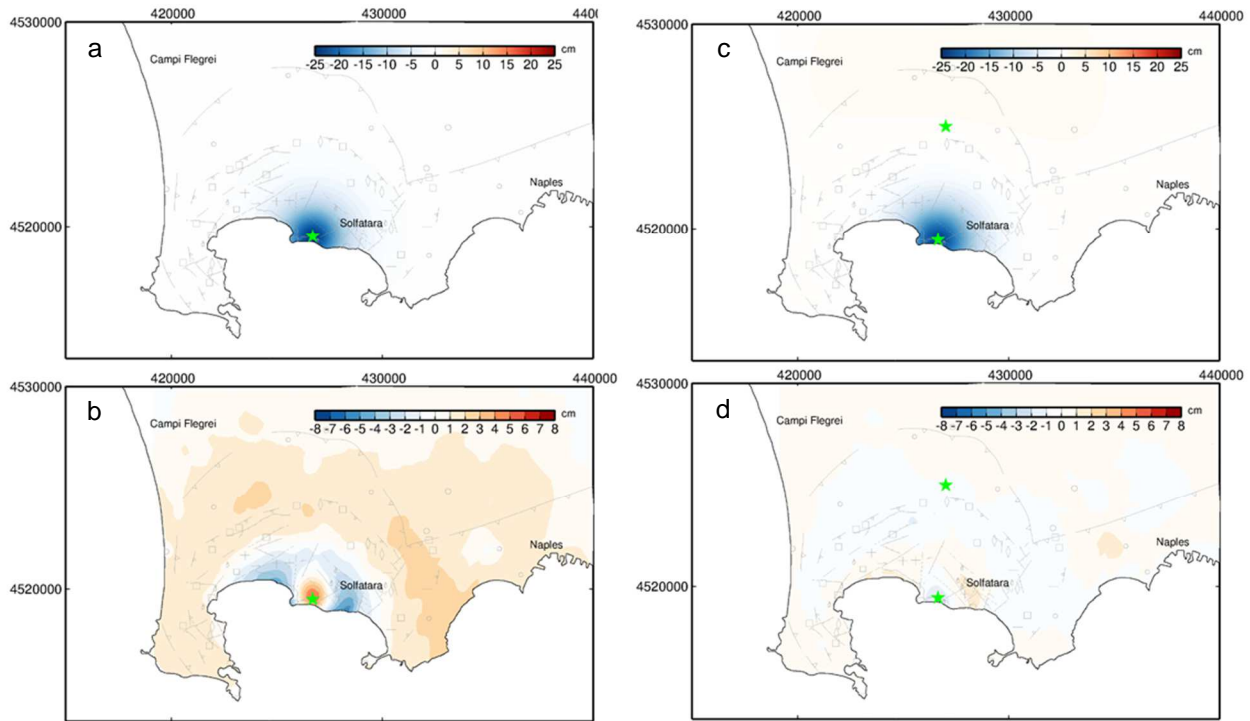


Figure 9: Modelled displacements and residuals in the vertical direction inverted for EOF12 for the time period 1993-1999 (subsidence). a) Displacements for a single source model, location shown by green star, at a depth of 1690 m; b) residuals between model shown in (a) and actual displacements (Figure 2); c) displacements for a two source model, locations shown by green stars, at depths of 2102 m (south, negative) and 14834 m (north, positive); d) residuals between model shown in (c) and actual displacements (Figure 2). All displacements and residuals in cm; source details are given in Table 2.

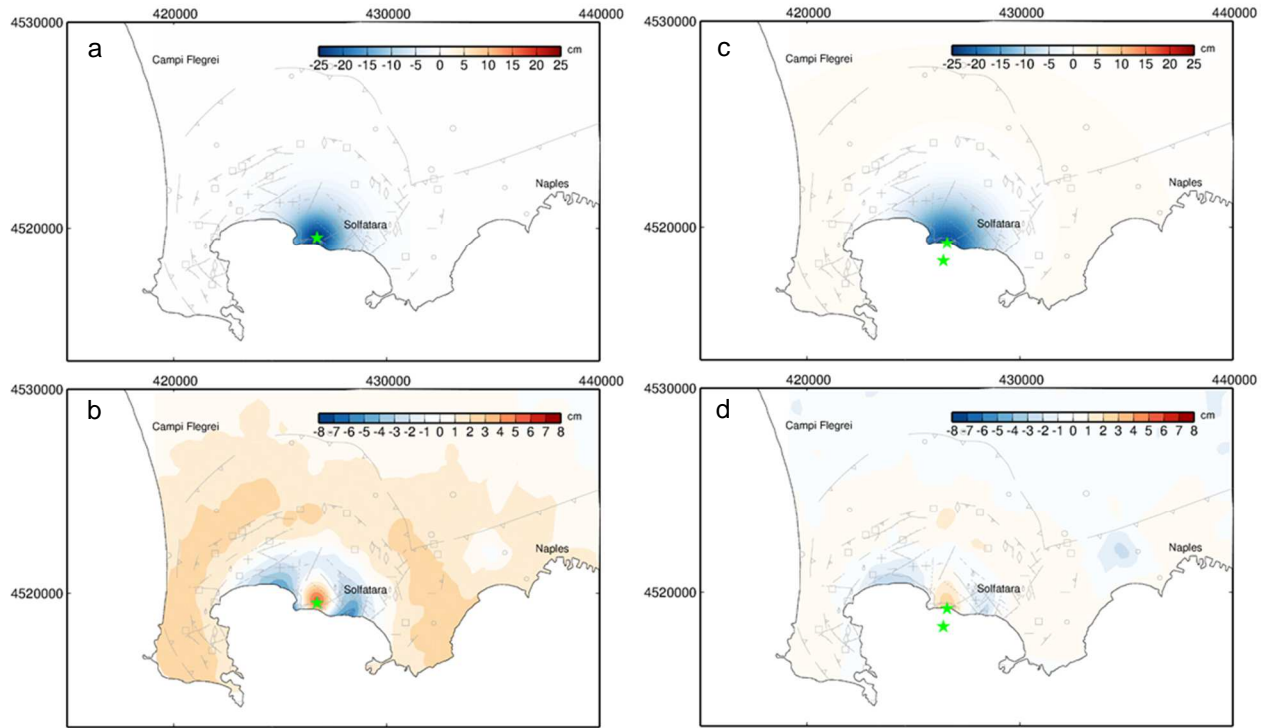


Figure 10: Modelled displacements and residuals in the vertical direction inverted for EOF123 for the time period 1993-1999 (subsidence). a) Displacements for a single source model, location shown by green star, at a depth of 1623 m; b) residuals between model shown in (a) and actual displacements (Figure 2); c) displacements for a two source model, locations shown by green stars, at depths of 2749 m (south, negative) and 8014 m (north, positive); d) residuals between model shown in (c) and actual displacements (Figure 2). All displacements and residuals in cm; source details are given in Table 2.

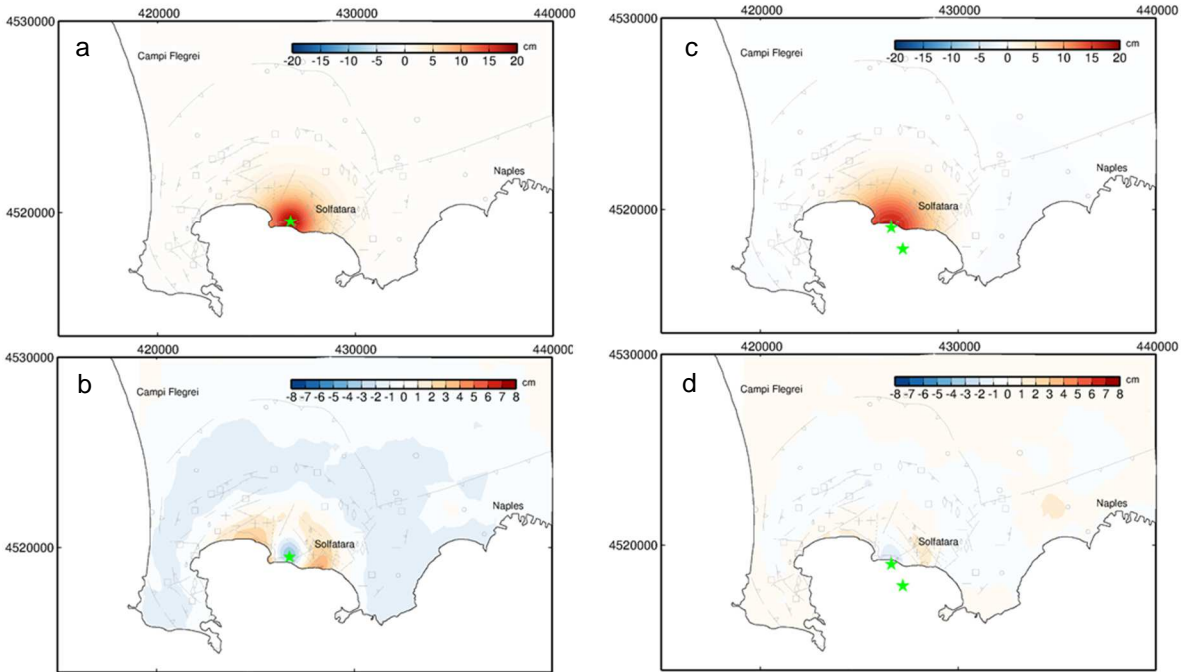


Figure 11: Modelled displacements and residuals in the vertical direction inverted for EOF1 for the time period 2007-2013 (uplift). a) Displacements for a single source model, location shown by green star, at a depth of 1671 m; b) residuals between model shown in (a) and actual displacements (Figure 2); c) displacements for a two source model, locations shown by green stars, at depths of 2892 m (south, positive) and 8454 m (north, negative); d) residuals between model shown in (c) and actual displacements (Figure 2). All displacements and residuals in cm; source details are given in Table 2.

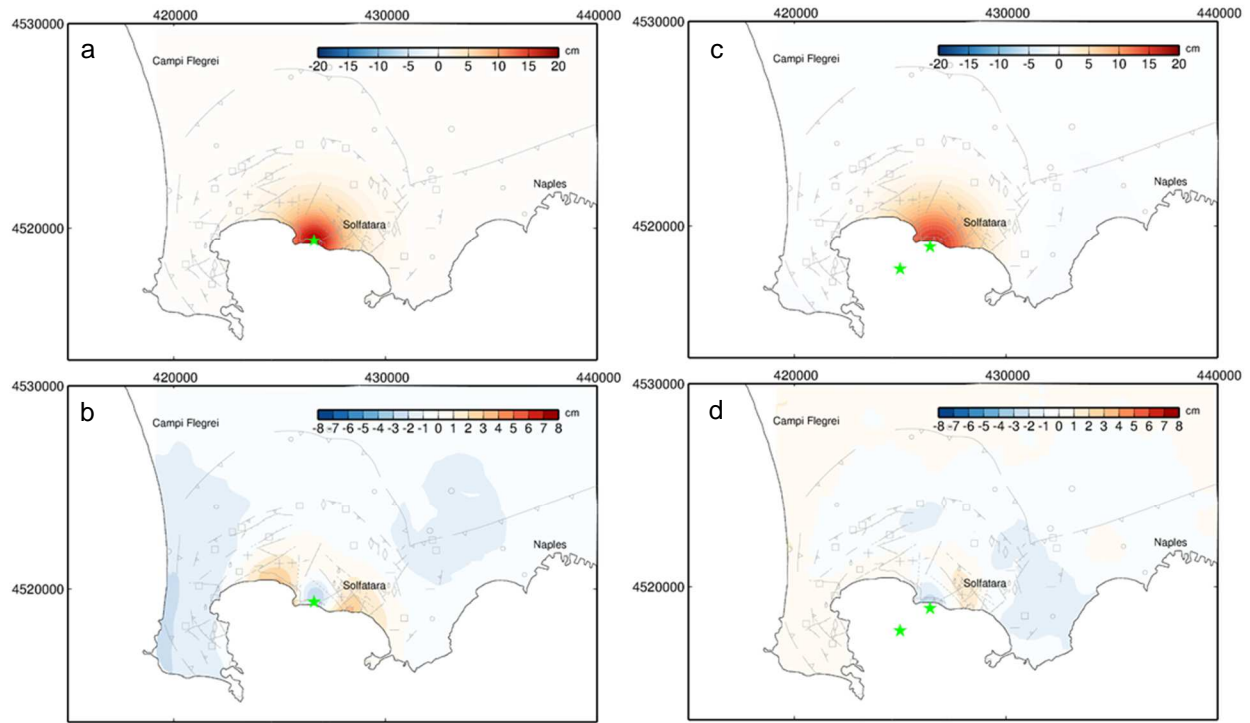


Figure 12: Modelled displacements and residuals in the vertical direction inverted for EOF12 for the time period 2007-2013 (uplift). a) Displacements for a single source model, location shown by green star, at a depth of 1810 m; b) residuals between model shown in (a) and actual displacements (Figure 2); c) displacements for a two source model, locations shown by green stars, at depths of 2818 m (south, positive) and 9340 m (north, negative); d) residuals between model shown in (c) and actual displacements (Figure 2). All displacements and residuals in cm; source details are given in Table 2.

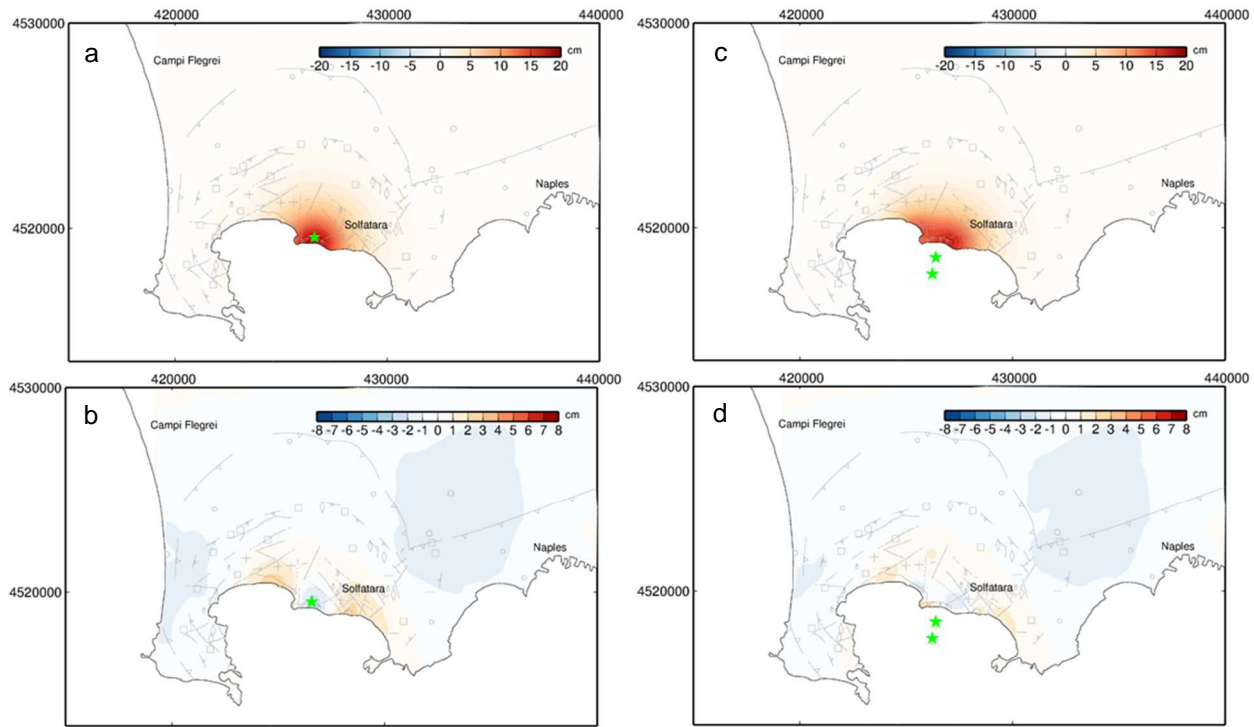


Figure 13: Modelled displacements and residuals in the vertical direction inverted for EOF123 for the time period 2007-2013 (uplift). a) Displacements for a single source model, location shown by green star, at a depth of 1987 m; b) residuals between model shown in (a) and actual displacements (Figure 2); c) displacements for a two source model, locations shown by green stars, at depths of 3402 m (south, positive) and 7624 m (north, negative); d) residuals between model shown in (c) and actual displacements (Figure 2). All displacements and residuals in cm; source details are given in Table 2.

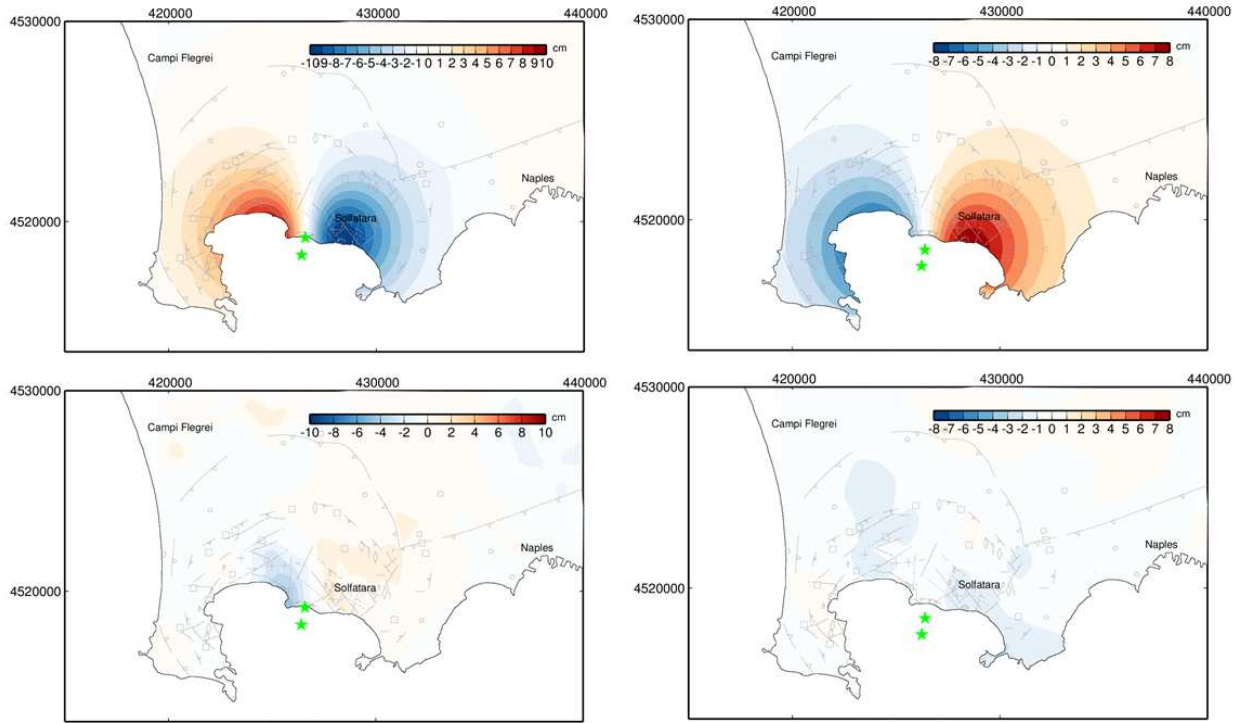


Figure 14: Modelled displacements and residuals in the east-west direction for the best fit two source model, using EOF123, as given in Table 2. a) Modelled displacements for a two source model, location shown by green star, for the 1993-1999 (subsidence); b) residuals between model shown in (a) and actual displacements (Figure 2b); c) displacements for the two source model, locations shown by green stars, for the time period 2007-2013 (uplift); d) residuals between model shown in (c) and actual displacements (Figure 2b). All displacements and residuals in cm.

Table 1: Seven DInSAR data sets providing continuous coverage from 1993 through 2013 used in this study. Included are incidence angle φ (degrees), azimuth angle θ (degrees), the number of available SLC SAR images, N , and the number of computed highly coherent interferograms, M .

| DInSAR data set | Orbit | Coverage period | θ | φ | N | M |
|--------------------|-------|-------------------|----------|-----------|-----|-----|
| ERS, Track 129 | asc | 19930110-20080917 | 344.1 | 23.2 | 90 | 215 |
| ERS, Track 036 | dsc | 19920608-20081225 | 194.1 | 23.2 | 84 | 164 |
| ENVISAT, Track 129 | asc | 20021113-20091216 | 344.0 | 22.8 | 46 | 120 |
| ENVISAT, Track 036 | dsc | 20030605-20101021 | 195.9 | 22.8 | 60 | 158 |
| R2, S3 | asc | 20090119-20130802 | 348.7 | 35.1 | 42 | 166 |
| R2, S3 | dsc | 20081227-20130803 | 190.4 | 35.1 | 53 | 290 |
| R2, F6 | asc | 20081229-20130805 | 351.0 | 48.3 | 50 | 158 |

911

912 Total $M = 1271$

913 Combined coverage: 1993/01/10-2013/08/03

914 Total number of unique time steps = 385 (48 repeated by different sensors)

915

Table 2: GA inversion results for different combinations of EOF modes for each time period, 1993-1999 (9399) and 2007-2013 (0713), and multiple source types. Here ‘Opposing’ refers to two sources with opposite polarity.

| Mode | | | | | | | | | | | |
|-------------|------|------------|----------|---------|--------|-------------------|----------|---------|--------|-------------------|--|
| Time period | RMS | Reduced | x-loc1 | y-loc1 | depth1 | ΔV | x-loc2 | y-loc2 | depth2 | ΔV | |
| Source type | (cm) | chi-square | (m UTM) | (m UTM) | (m) | (m ³) | (m UTM) | (m UTM) | (m) | (m ³) | |
| EOF1 | | | | | | | | | | | |
| 0713 | | | | | | | | | | | |
| One source | 0.88 | 76 | 426727.7 | 4519507 | 1671 | 498850 | N/A | N/A | N/A | N/A | |
| Two source | 0.88 | 76 | 426726.4 | 4519510 | 1679 | 495814 | 429994.7 | 4534989 | 12839 | 4188.8 | |
| Opposing | 0.68 | 45 | 426623.9 | 4519007 | 2892 | 1831470 | 427207.2 | 4517885 | 8454 | -3764178.3 | |
| 9399 | | | | | | | | | | | |
| One source | 1.51 | 251 | 426729.2 | 4519518 | 1665 | -681793 | N/A | N/A | N/A | N/A | |
| Two source | 1.52 | 257 | 426733.5 | 4519523 | 1675 | -685546 | 429850.4 | 4534926 | 14947 | -65449.8 | |
| Opposing | 1.01 | 112 | 426679.0 | 4519452 | 2069 | -1062394 | 427273.6 | 4525027 | 13802 | 3434913.4 | |
| EOF12 | | | | | | | | | | | |
| 0713 | | | | | | | | | | | |
| One source | 0.81 | 76 | 426628.2 | 4519374 | 1810 | 599211 | N/A | N/A | N/A | N/A | |
| Two source | 0.81 | 79 | 425512.9 | 4519377 | 1805 | 599211 | 429906.2 | 4534986 | 14969 | 66238.3 | |
| Opposing | 0.51 | 25 | 426417.4 | 4518949 | 2818 | 1683618 | 425000.8 | 4517856 | 9340 | -3380160.2 | |
| 9399 | | | | | | | | | | | |
| One source | 1.51 | 255 | 426706.1 | 4519497 | 1690 | -704517 | N/A | N/A | N/A | N/A | |
| Two source | 1.52 | 259 | 426689.1 | 4519439 | 1690 | -712203 | 429984.1 | 4534950 | 14969 | -69455.8 | |
| Opposing | 1.00 | 114 | 426656.0 | 4519441 | 2102 | -1087768 | 427021.8 | 4525006 | 14834 | 3822992.5 | |
| EOF123 | | | | | | | | | | | |
| 0713 | | | | | | | | | | | |
| One source | 0.78 | 82 | 426576.2 | 4519232 | 1987 | 723836 | N/A | N/A | N/A | N/A | |
| Two source | 0.80 | 82 | 426572.4 | 4519232 | 2003 | 727741 | 427482.1 | 4510122 | 5055 | 67033.2 | |
| Opposing | 0.32 | 14 | 426394.7 | 4518504 | 3402 | 2942928 | 426234.9 | 4517698 | 7624 | -4113840.0 | |
| 9399 | | | | | | | | | | | |
| One source | 1.51 | 244 | 426733.1 | 4519531 | 1623 | -652261 | N/A | N/A | N/A | N/A | |
| Two source | 1.51 | 250 | 426733.6 | 4519526 | 1656 | -666918 | 427014.1 | 4510018 | 13897 | -35561.4 | |
| Opposing | 0.57 | 43 | 426583.2 | 4519206 | 2749 | -2250847 | 426410.1 | 4518333 | 8014 | 4630734.3 | |